Subsidence at Cerro Prieto Geothermal Field and postseismic slip along the Indiviso fault from 2011 to 2016 RADARSAT-2 DInSAR time series analysis

Sergey V. Samsonov[1], Wanpeng Feng[1] (ID), and Yuri Fialko[2] (ID)

[1]Canada Centre for Mapping and Earth Observation, Natural Resources Canada, Ottawa, Ontario, Canada, [2]Institute of Geophysics and Planetary Physics, Scripps Institution of Oceanography, University of California, San Diego, La Jolla, California, USA

Abstract We present RADARSAT-2 Differential Interferometric Synthetic Aperture Radar (DInSAR) observations of deformation due to fluid extraction at the Cerro Prieto Geothermal Field (CPGF) and afterslip on the 2010 $M7.2$ El Mayor-Cucapah (EMC) earthquake rupture during 2011–2016. Advanced multidimensional time series analysis reveals subsidence at the CPGF with the maximum rate greater than 100 mm/yr accompanied by horizontal motion (radial contraction) at a rate greater than 30 mm/yr. During the same time period, more than 30 mm of surface creep occurred on the Indiviso fault ruptured by the EMC earthquake. We performed inversions of DInSAR data to estimate the rate of volume changes at depth due to the geothermal production at the CPGF and the distribution of afterslip on the Indiviso fault. The maximum coseismic slip due to the EMC earthquake correlates with the Coulomb stress changes on the Indiviso fault due to fluid extraction at the CPGF. Afterslip occurs on the periphery of maximum coseismic slip areas. Time series analysis indicates that afterslip still occurs 6 years after the earthquake.

1. Introduction

Anthropogenic fluid extraction and injection are often accompanied by small to moderate size earthquakes [*Segall et al.*, 1994; *Fialko and Simons*, 2000; *Keranen et al.*, 2014; *McNamara et al.*, 2015; *Shirzaei et al.*, 2016]. In tectonically active regions, stress and pore pressure perturbations due to anthropogenic activities may also trigger large earthquakes [*Mulargia and Bizzarri*, 2014]. Investigating the relationships between fluid extraction and deformation of the host rocks (including induced seismicity and aseismic fault slip) can provide useful insights into how rocks respond in situ to controlled forcing. Differential Interferometric Synthetic Aperture Radar (DInSAR) is well suited for mapping spatial extent, magnitude, and evolution of anthropogenic deformation, thanks to high measurement precision and high spatial resolution over large areas [e.g., *Samsonov et al.*, 2013, 2014a, 2014b, 2015, 2016]. In this paper we investigate possible relationships between deformation caused by geothermal production at the Cerro Prieto plant (Baja California, Mexico) and the nearby 2010 magnitude 7.2 El Mayor-Cucapah earthquake.

The world second-largest Cerro Prieto geothermal power station exploits the Cerro Prieto Geothermal Field (CPGF). At the CPGF geothermal fluid has been extracted since 1973 from depths of 1.5–3.0 km at a rate of approximately 6.3×10^7 m^3/yr; 90% of extracted fluid is recovered by reinjection and natural recharge [*Trugman et al.*, 2014]. The fluid net loss causes ground deformation, predominantly subsidence over approximately 25 km × 25 km area. The first evidence of subsidence came from the precise leveling surveys performed during 1977–1997; *Glowacka et al.* [1999] observed that subsidence rate scales with the volume of the extracted fluid. The ERS-1/2 DInSAR studies performed by *Carnec and Fabriol* [1999] and *Hanssen* [2006] showed up to 15 mm/month subsidence in the production zone during 1993–1997 and 1995–1997, respectively. *Sarychikhina et al.* [2011] based on analysis of 2003–2006 ENVISAT data detected subsidence in the production (11 cm/yr) and recharge (17 cm/yr) zones and proposed that the spatial extent of subsidence is controlled by tectonic faults. *Sarychikhina et al.* [2011] also estimated the total rate of volumetric contraction due to fluid extraction of 1.24×10^7 m^3/yr. *Trugman et al.* [2014] based on 2006–2009 ALOS data and modeling using Mogi sources estimated the rate of volumetric contraction due to fluid extraction of 9×10^6 m^3/yr.

The 4 April 2010 $M_w 7.2$ El Mayor-Cucapah (EMC) earthquake [*Wei et al.*, 2011] occurred in a close proximity to the geothermal production area (Figure 1). The EMC earthquake ruptured a 120 km long system of faults
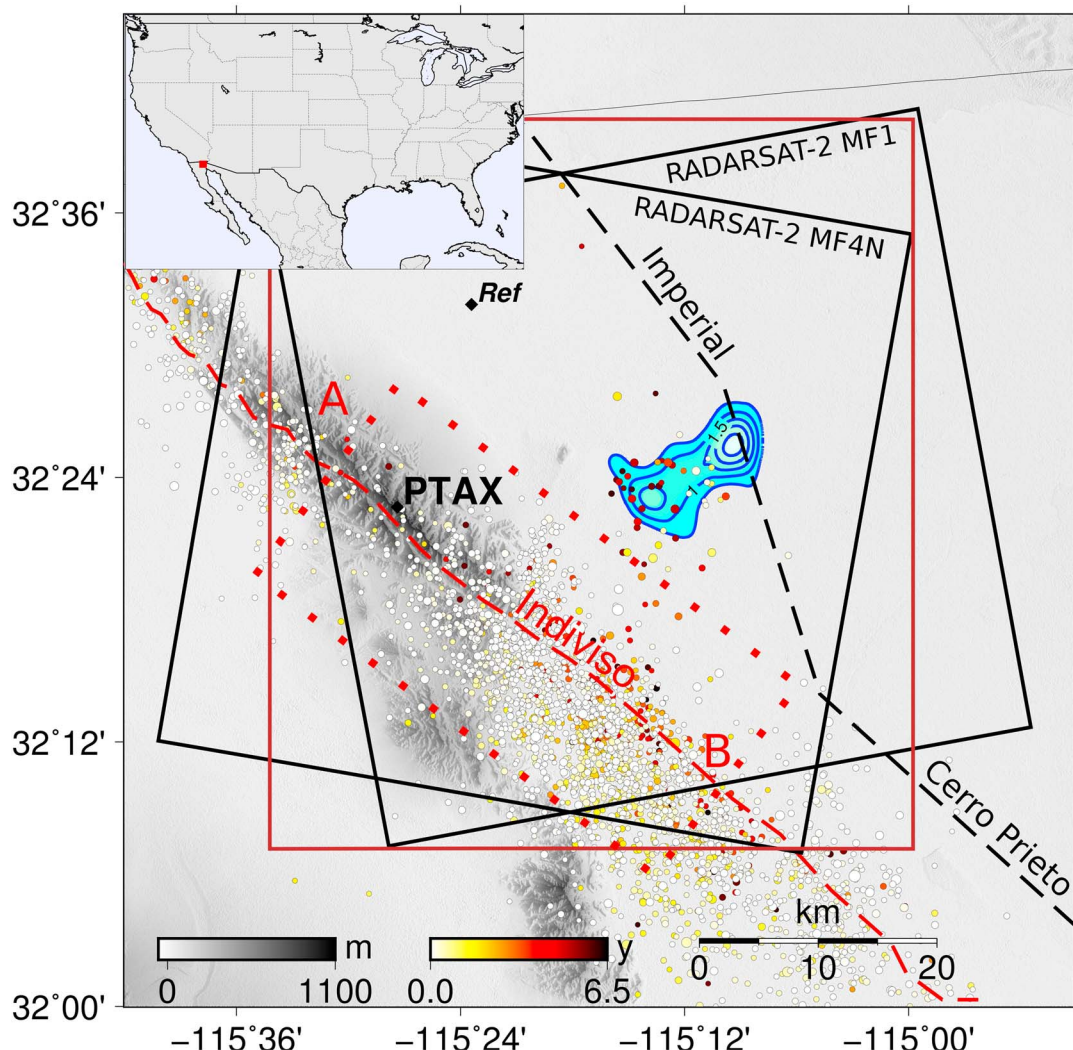
Figure 1. Map of the area of study. The rupture trace of the El Mayor-Cucapah earthquake is denoted by a red dashed line [*Gonzalez-Ortega et al.*, 2014]. Stress changes are estimated on a segment outlined by a red dotted rectangle. Footprints of RADARSAT-2 ascending and descending SAR images are denoted by black rectangles. A brown rectangle denotes an area shown in Figure 2. Black diamond denote permanent GPS site. Circles denote earthquakes, color coded by date since 4 June 2010 (from the U.S. Geological Survey (USGS) catalog). Grey color denotes topography. Blue contour lines denote the inferred volume changes at depth ($\times 10^6$ m^3), due to fluid extraction at the CPGF between 1 October 2011 and 24 July 2016. Imperial and Cerro Prieto faults are denoted by a black dashed line (from the USGS tectonic plate boundary database).

including the previously unknown Indiviso fault [*Gonzalez-Ortega et al.*, 2014]. The maximum coseismic slip occurred at 2–4 km depth next to the CPGF. *Trugman et al.* [2014] showed that the Coulomb stressing rate at the earthquake hypocenter due to fluid extraction at the CPGF is comparable to the tectonic loading rate and suggested that the EMC earthquake may have been triggered by the geothermal production. The earthquake was followed by a robust afterslip on the EMC rupture [*Gonzalez-Ortega et al.*, 2014]. Unfortunately, ENVISAT and ALOS satellites stopped acquiring data shortly after the earthquake, hampering studies of postseismic response.

Here we present Synthetic Aperture Radar data acquired by the RADARSAT-2 satellite mission during 1 October 2011 to 24 July 2016. We computed two-dimensional (2-D) displacement time series by decomposing the line-of-sight DInSAR measurements from the ascending and descending satellite orbits. These data provide unique constraints on deformation processes due to fluid pumping at Cerro Prieto and the EMC earthquake rupture over a time period when no other DInSAR data are available. We use DInSAR observations

Table 1. RADARSAT-2 Synthetic Aperture Radar Data Used in This Study: θ Is Azimuth and ϕ Is Incidence Angle, N Is Number of Images, and M Is Number of Interferograms Computed for Each Data Set

| DInSAR Set	Orbit	UTM	Coverage	θ (deg)	ϕ (deg)	N	M
RADARSAT-2, MF1	asc	01:43	20110913–20160724	349.4	38.4	53	434
RADARSAT-2, MF4N	dsc	13:36	20111001–20160811	−170.3	44.0	58	344
Total:			20111001–20160724			109	778

to quantify subsidence due to geothermal production and afterslip on the EMC rupture. We also compute Coulomb stress changes on the Indiviso fault due to fluid extraction at the CPGF and demonstrate that the area of maximum coseismic slip correlates with positive Coulomb stress.

2. Data: Processing Methodology and Results

We used 53 ascending Multi-Look Fine 1 (MF1) and 58 descending Multi-Look Fine 4N (MF4N) Single-Look Complex (SLC) RADARSAT-2 images with the spatial extent of 50 km × 50 km and the spatial resolution of 3.1 m × 4.6 m in range and azimuth, respectively (Figures 1 and S1 in the supporting information, and Table 1). The standard DInSAR processing was performed with the GAMMA software [*Wegmuller and Werner*, 1997]. A single master for each data set was selected, and remaining SLC slave images were coregistered and resampled to the master geometry. The topographic phase was computed using the 30 m resolution Shuttle Radar Topography Mission Digital Elevation Model [*Rabus et al.*, 2003] and removed from the interferograms.
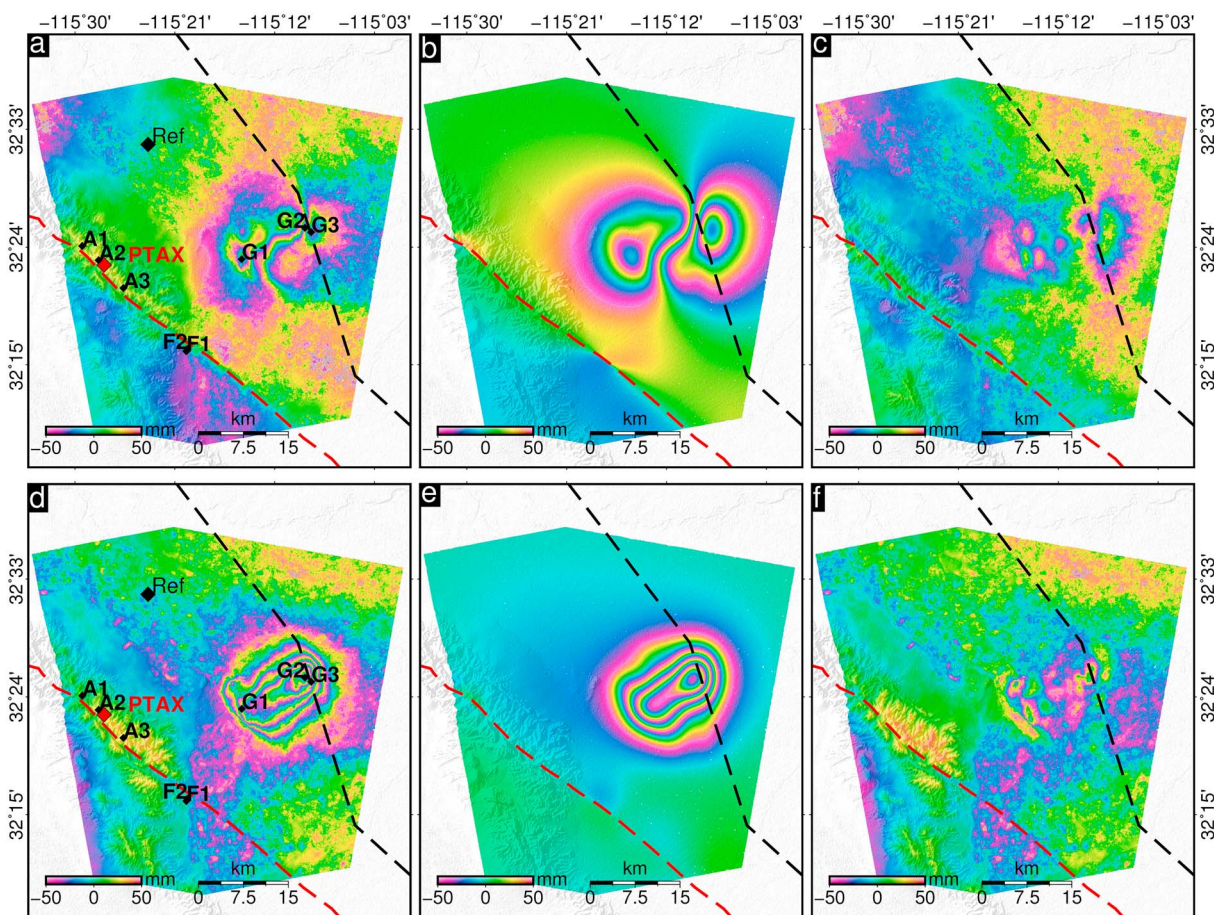
Figure 2. (a, d) Observed, (b, e) modeled, and (c, f) residual surface displacements that occurred during 1 October 2011 to 24 July 2016. East-west component is shown in Figures 2a–2c; vertical component is shown in Figures 2d–2f. Points G1–G3 mark areas of fastest motion at CPGF. Points A1–A3 mark high-altitude areas with large seasonal atmospheric signal. Points F1–F2 mark an area with the sharpest discontinuity across fault. Ref is reference point.
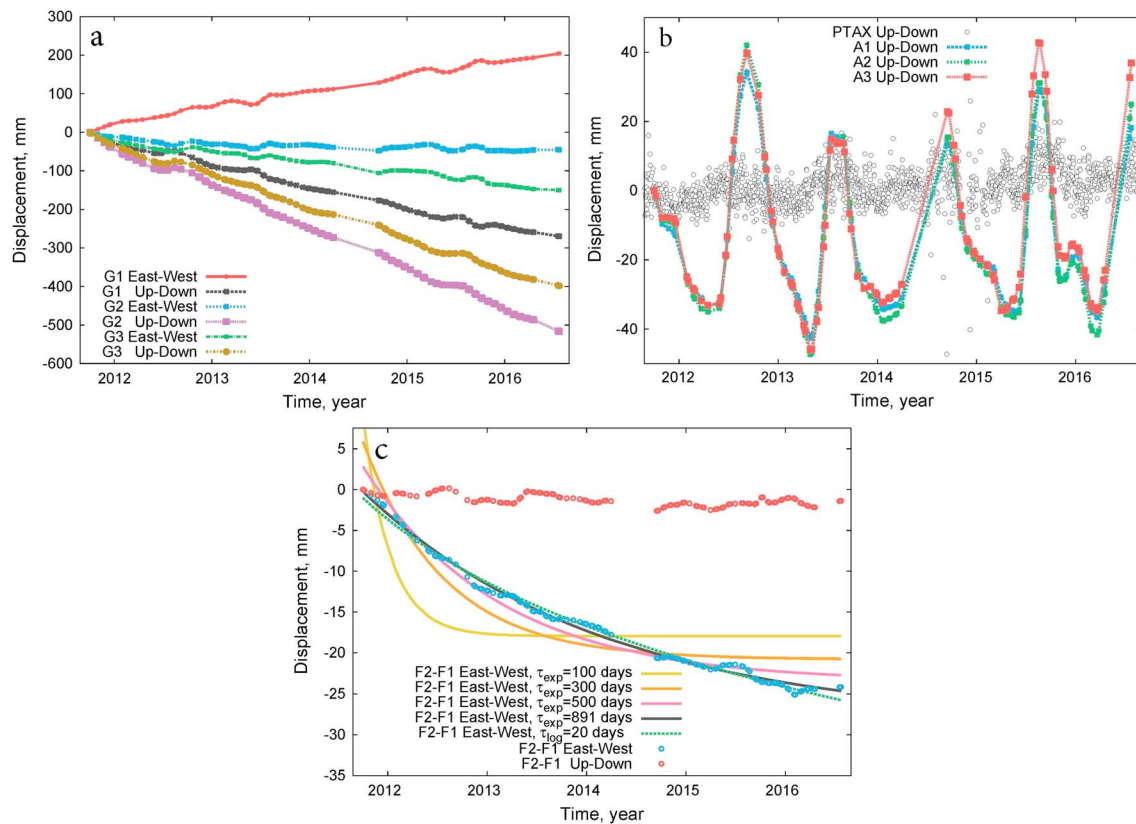
Figure 3. (a) East-west and vertical displacement time series computed with MSBAS for G1–G3, (b) vertical time series for A1–A3 and PTAX, (c) east-west and vertical time series for F2 referenced to F1 (i.e., F2–F1). Various exponential and logarithmic models are fitted to the east-west component of relative motion between F1 and F2.

Adaptive filtering [*Goldstein and Werner*, 1998], phase unwrapping [*Costantini*, 1998], and geocoding procedures were applied. Interferograms were also corrected for long-wavelength ramps (e.g., due to imprecise orbits). The resulting 434 ascending and 344 descending interferograms were resampled to a common spatial grid with 20 m resolution and processed with the advanced Multidimensional Small Baseline Subset (MSBAS) software [*Samsonov and d'Oreye*, 2012; *Samsonov et al.*, 2014c, 2014d, 2014b, 2016] to generate the times series of vertical and horizontal (east-west) components of surface displacements for each coherent pixel.

The cumulative deformation maps from 1 October 2011 to 24 July 2016 (Figure 2) show 520 mm of subsidence at the CPGF accompanied by 180 mm of horizontal east-west motion, corresponding to mean velocities of 108 mm/yr and 37 mm/yr, respectively. The subsiding area has an approximately elliptical shape with the major axis along the NE-SW direction. The fastest subsidence is observed in the NE part of the CPGF, consistent with the results of *Sarychikhina et al.* [2011]. The horizontal displacements exhibit motion toward the center of subsidence, which is typical for the contraction sources [e.g., *Fialko and Simons*, 2000; *Fialko et al.*, 2001; *Samsonov et al.*, 2016]. During the same period, the horizontal east-west displacements in the vicinity of the Indiviso fault (red dashed line [*Gonzalez-Ortega et al.*, 2014]) show a discontinuity of approximately 30 mm, corresponding to an average slip velocity of 9 mm/yr. The largest displacement gradient is observed approximately at the center of the plotted fault segment, in the close proximity to the CPGF (Figure 2).

Time series of ground deformation for a few characteristic regions are shown in Figure 3. At the CPGF, point G1 corresponds to a region experiencing fastest eastward motion, point G3 corresponds to fastest westward motion, and point G2 corresponds to fastest subsidence. One can see that surface deformation within the CPGF occurred at an approximately constant rate; also some small-amplitude deviations are seen in the data (Figure 3). In the Cucapah mountain area west of the CPGF, points A1–A3 correspond to the elevated region, at which very large seasonal atmospheric signal with an amplitude of up to ±50 mm is observed in time series.

Similar seasonal signals were previously reported and discussed by *Samsonov et al.* [2014d]. The vertical component of GPS time series from a nearby site PTAX also shows a seasonal signal, but with a much smaller amplitude (∼3 mm, Figure 3b).

Points F1 and F2 are located on the opposite sides of the El Mayor-Cucapah earthquake rupture in area of a high gradient in the east-west displacement component. High gradients in surface displacements seen in the DInSAR data (Figure 2a) signify shallow creep on the earthquake rupture. Time series of displacements between points F1 and F2 (Figure 3c) reveal a decaying transient, consistent with afterslip on the earthquake rupture. We compared the observed time-dependent fault slip history with simple exponential and logarithmic models used to fit postseismic data covering first few years after the earthquake [*Gonzalez-Ortega et al.*, 2014]. Models assuming an exponential decay with characteristic times of the order of a few months [*Gonzalez-Ortega et al.*, 2014] disagree with the extended time series and can be clearly ruled out by the data (Figure 3c). In contrast, a range of models assuming a logarithmic decay, including models with the characteristic decay time of 20 days [*Gonzalez-Ortega et al.*, 2014], are able to fit the time series. Because the parametric fits assume an origin time on the date of the EMC earthquake, there is a trade-off between the total amplitude of the signal and the characteristic decay time, so that neither parameter can be determined uniquely by fitting a partial time series.

3. Modeling

Maps of cumulative displacements that occurred between 1 October 2011 and 24 July 2016 were used as input for modeling. Fluid withdrawal at the CPGF and postseismic slip on the EMC rupture were modeled simultaneously using analytic solutions for dislocations in an elastic half-space *Okada* [1985, 1992]. We assumed that contributions from other relaxation mechanisms are negligible. In particular, viscoelastic relaxation cannot produce high gradients in surface displacements across the fault trace (Figure 2a). The data shown in Figure 2 also do not exhibit similarities with predictions of models of poroelastic deformation [*Gonzalez-Ortega et al.*, 2014].

Surface subsidence due to fluid extraction at the CPGF was modeled using 324 deflation point sources [*Okada*, 1992] distributed on 1 km × 1 km grid at 2.7 km depth [e.g., *Trugman et al.*, 2014]. Modeling of postseismic slip on the EMC rupture used the fault geometry and discretization from the study of *Gonzalez-Ortega et al.* [2014]. The depth-dependent fault discretization, with the patch size varying from ∼0.8 km near the surface to ∼6.0 km, ensures a nearly uniform model resolution [*Fialko*, 2004]. The resulting linear system of equations is

$$\begin{pmatrix} G1 & G2 \\ \Delta^2 L1 & 0 \\ 0 & \Delta^2 L2 \end{pmatrix} \begin{pmatrix} V \\ S \end{pmatrix} = \begin{pmatrix} d \\ 0 \\ 0 \end{pmatrix} \qquad (1)$$

where matrices $G1$ and $G2$ represent Green functions for volume changes V of the deflation point sources and afterslip S on the earthquake fault, respectively; $L1$ and $L2$ are the smoothing kernels based on a finite difference approximation of the Laplacian operator; Δ^2 is the smoothing factor; and d is the data vector (vertical and horizontal displacements). Inversions were performed using the geodetic inversion package PSOKINV [*Feng et al.*, 2016] based on the nonnegative least squares method of *Ward and Barrientos* [1986].

The best fitting distribution of volume changes at depth is shown in Figure 1 (blue contours), and modeled ground deformation due to the deflation point sources are shown in Figure S2. As expected, the inferred distribution of deflation resembles the shape of surface subsidence (Figure 2d). The maximum volume change for the individual deflation sources is greater than 2×10^6 m^3. The total volume change during the 4.8 years period of observations is 1.1×10^8 m^3, corresponding to an average rate of deflation of 2.2×10^7 m^3/yr. The latter is 2.4 times larger than the deflation rate estimated by *Trugman et al.* [2014] (9×10^6 m^3/yr) from the analysis of ALOS data spanning a time period 2006–2009. This difference in part may stem from the fact that the data used by *Trugman et al.* [2014] do not cover the entire CPGF area and may have a lower precision due to a smaller number of SAR acquisitions (23 versus 109). Another possibility is that the average rate of subsidence varied over the respective time periods (2006–2009 versus 2011–2016).

Results of inversions show that afterslip on the earthquake rupture primarily occurs around the areas of maximum coseismic slip (Figure 4b), consistent with previous studies of postseismic deformation due to the EMC earthquake [*Gonzalez-Ortega et al.*, 2014], as well as other earthquakes on the San Andreas Fault system and
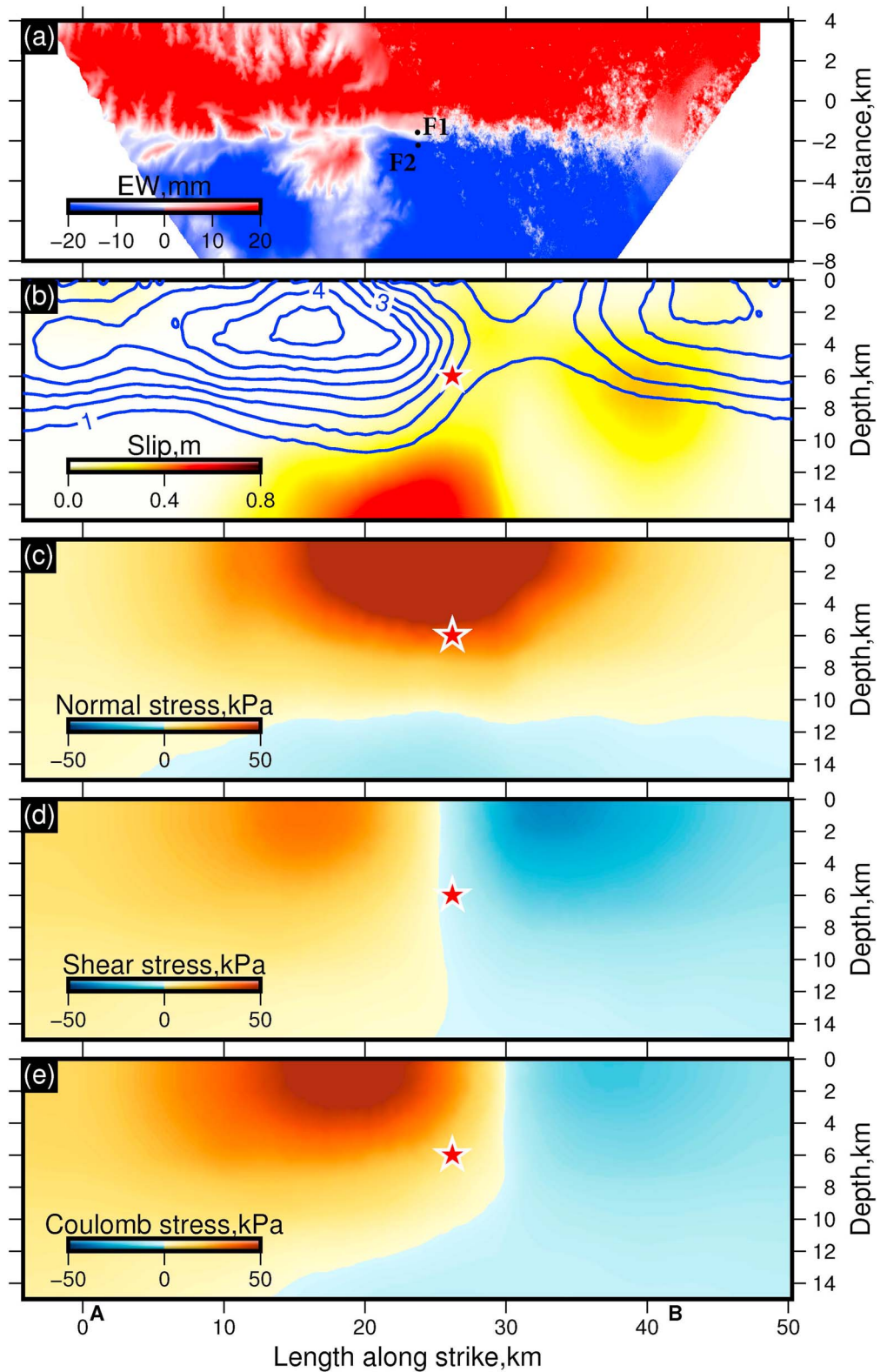
Figure 4. (a) Surface map of east-west displacements between 1 October 2011 and 24 July 2016; (b) coseismic slip due to El Mayor-Cucapah earthquake (contour lines) [*Gonzalez-Ortega et al.*, 2014] and afterslip during 1 October 2011 to 24 July 2016 (color) from this study. Components of stress change due to groundwater extraction at CPGF on the EMC rupture: (c) normal; (d) shear; and (e) Coulomb. Positive values of Coulomb stress change encourage right-lateral slip. Star shows location of the hypocenter [*Wei et al.*, 2011].

elsewhere [e.g., *Barbot et al.*, 2008, 2009; *Hsu et al.*, 2006; *Yamagiwa et al.*, 2015]. Some shallow afterslip occurs between coseismic asperities (e.g., along-strike coordinates 30–40 km in Figure 4b) where points F1 and F2 were selected (Figure 2a). Deep afterslip is concentrated below the largest coseismic asperity near the earthquake hypocenter [*Wei et al.*, 2011]. Modeled ground deformation due to the afterslip is shown in the supporting information Figure S3.

In order to quantify the impact of fluid extraction at the CPGF on the EMC rupture, we calculated the normal, shear, and Coulomb stress changes at the center of each patch of the discretized EMC rupture using the three-dimensional dislocation model of *Okada* [1992]. We assumed the Young's modulus of 40 GPa and the effective frictional coefficient of 0.4 [*Simpson and Reasenberg*, 1994]. The respective stress perturbations are shown in Figures 4c–4e (projected on a vertical plane) and supporting information Figures S6 and S7 (3-D perspective view).

We additionally simulated interseismic deformation due to the Imperial and Cerro Prieto faults, assuming slip rate of 40 mm/yr and locking depth of 10 km [*Bennett et al.*, 1996]. The fault traces were taken from the USGS tectonic plate boundary database. The results are shown in supporting information Figures S4 and S5, and cumulative displacement and velocity for selected regions are given in Table S1. Within our study area, interseismic deformation is small compared to contributions from CPGF and afterslip on the EMC rupture.

4. Discussion and Conclusions

Mean line-of-sight velocities computed with the standard Small Baseline Subset algorithm [*Berardino et al.*, 2002] can be decomposed into the vertical and east-west components, provided data are available from more than one look direction [e.g., *Manzo et al.*, 2006]. However, this approach is valid only if deformation rates are constant. Time series computed with the MSBAS method can accurately estimate two components of time-dependent displacements, e.g., due to postseismic deformation or fluid withdrawal (Figure 3). A limitation of the MSBAS method is that it neglects the north-south component of deformation. This however has little effect on the accuracy of the vertical and east-west components, provided the magnitude of the north-south component is comparable to or smaller than the magnitude of the other two components of the displacement vector [*Samsonov and d'Oreye*, 2012].

MSBAS analysis of the RADARSAT-2 data covering the 2010 El Mayor-Cucapah earthquake area reveals a robust afterslip on the earthquake rupture that is still occurring 6 years after the earthquake (Figure 3c). This is similar to afterslip transients documented for other large earthquakes [e.g., *Hsu et al.*, 2006; *Barbot et al.*, 2009; *Wang and Fialko*, 2014]. A comparison of the coseismic and postseismic slip distributions on the EMC rupture to stress changes due to fluid extraction at the CPGF (Figure 4) suggests that the latter may not only have advanced the timing of the main shock [*Trugman et al.*, 2014] but also affected the seismic moment release, such that fault areas that experienced the largest increase in Coulomb stress produced the largest slip during the EMC earthquake. To quantify this relationship, we computed the coefficients of correlation R and determination R^2 [*Wackerly et al.*, 2007] between the coseismic slip due to the EMC earthquake and the Coulomb stress change due to geothermal production. The respective values are 61% (p value $\ll 0.05$) and 37% (p value $\ll 0.05$). R^2 describes the proportion of the variance in the dependent variable (coseismic slip) that is predictable from the independent variable (the Coulomb stress change). The correlation coefficient is sufficiently high to indicate a possible relationship between the stress changes due to the geothermal production and the coseismic slip distribution. Stress changes due to fluid extraction may have also affected postseismic slip, in particular on the shallow part of the Indiviso fault just south of the earthquake hypocenter (Figure 4). In contrast, deep afterslip appears to be primarily driven by the coseismic stress changes.

It should be noted that the predicted stress changes due to fluid extraction are model dependent. For example, models that use a distribution of horizontal Mode I dislocations [*Okada*, 1992] approximating a deflating horizontal crack [*Fialko et al.*, 2001] are able to fit subsidence at the CPGF equally well but give rise to an opposite sign of the normal stress change on the EMC rupture (i.e., compression instead of extension) in the vicinity of the geothermal field.

Assuming that a distribution of isotropic deflation sources is an adequate model of volume changes due to geothermal production at the CPGF, results of our inversions of RADARSAT-2 DInSAR data support a conclusion that anthropogenic activities at the CPGF may have contributed to triggering of the 2010 El Mayor-Cucapah earthquake and affected both coseismic and postseismic slip on the earthquake rupture.

References

Barbot, S., Y. Hamiel, and Y. Fialko (2008), Space geodetic investigation of the coseismic and postseismic deformation due to the 2003 $M(w)$7.2 Altai earthquake: Implications for the local lithospheric rheology, *J. Geophys. Res.*, *113*, B03403, doi:10.1029/2007JB005063.

Barbot, S., Y. Fialko, and Y. Bock (2009), Postseismic deformation due to the M_w6.0 2004 Parkfield earthquake: Stress-driven creep on a fault with spatially variable rate-and-state friction parameters, *J. Geophys. Res.*, *114*, B07405, doi:10.1029/2008JB005748.

Bennett, R., W. Rodi, and R. Reilinger (1996), Global Positioning System constraints on fault slip rates in Southern California and northern Baja, Mexico, *J. Geophys. Res.*, *101*(B10), 21,943–21,960, doi:10.1029/96JB02488.

Berardino, P., G. Fornaro, and R. Lanari (2002), A new algorithm for surface deformation monitoring based on small baseline differential SAR interferograms, *IEEE Trans. Geosci. Remote Sens.*, *40*(11), 2375–2383.

Carnec, C., and H. Fabriol (1999), Monitoring and modeling land subsidence at the Cerro Prieto Geothermal Field, Baja California, Mexico, using SAR interferometry, *Geophys. Res. Lett.*, *26*(9), 1211–1214, doi:10.1029/1999GL900062.

Costantini, M. (1998), A novel phase unwrapping method based on network programming, *IEEE Trans. Geosci. Remote Sens.*, *36*(3), 813–821.

Feng, W., E. Lindsey, S. Barbot, S. V. Samsonov, K. Li, P. Li, Z. Li, R. Almeida, J. Chen, and X. Xu (2016), Source characteristics of the 2015 M_w7.8 Gorkha earthquake and its M_w 7.2 aftershock from space geodesy, *Tectonophysics*, doi:10.1016/j.tecto.2016.02.029.

Fialko, Y. (2004), Probing the mechanical properties of seismically active crust with space geodesy: Study of the co-seismic deformation due to the 1992 M_w7.3 Landers (Southern California) earthquake, *J. Geophys. Res.*, *109*, B03307, doi:10.1029/2003JB002756.

Fialko, Y., and M. Simons (2000), Deformation and seismicity in the Coso Geothermal Area, Inyo County, California: Observations and modeling using satellite radar interferometry, *J. Geophys. Res.*, *105*(B9), 21,781–21,793, doi:10.1029/2000JB900169.

Fialko, Y., Y. Khazan, and M. Simons (2001), Deformation due to a pressurized horizontal circular crack in an elastic half-space, with applications to volcano geodesy, *Geophys. J. Int.*, *146*(1), 181–190, doi:10.1046/j.1365-246X.2001.00452.x.

Glowacka, E., J. González, and H. Fabriol (1999), Recent vertical deformation in Mexicali Valley and its relationship with tectonics, seismicity, and the exploitation of the Cerro Prieto Geothermal Field, Mexico, *Pure Appl. Geophys.*, *156*(4), 591–614, doi:10.1007/s000240050314.

Goldstein, R., and C. Werner (1998), Radar interferogram filtering for geophysical applications, *Geophys. Res. Lett.*, *25*(21), 4035–4038.

Gonzalez-Ortega, A., Y. Fialko, D. Sandwell, F. Nava-Pichardo, J. Fletcher, J. Gonzalez-Garcia, B. Lipovsky, M. Floyd, and G. Funning (2014), El Mayor-Cucapah (M_w7.2) earthquake: Early near-field postseismic deformation from InSAR and GPS observations, *J. Geophys. Res. Solid Earth*, *119*, 1482–1497, doi:10.1002/2013JB010193.

Hanssen, R. (2006), *Radar Interferometry Data Interpretation and Error Analysis*, Springer, Netherlands.

Hsu, Y.-J., M. Simons, J.-P. Avouac, J. Galetzka, K. Sieh, M. Chlieh, D. Natawidjaja, L. Prawirodirdjo, and Y. Bock (2006), Frictional afterslip following the 2005 Nias-Simeulue earthquake, Sumatra, *Science*, *312*(5782), 1921–1926, doi:10.1126/science.1126960.

Keranen, K., M. Weingarten, G. Abers, B. Bekins, and S. Ge (2014), Sharp increase in central Oklahoma seismicity since 2008 induced by massive wastewater injection, *Science*, *345*(6195), 448–451, doi:10.1126/science.1255802.

Manzo, M., G. Ricciardi, F. Casu, G. Ventura, G. Zeni, S. Borgstrom, P. Berardino, C. Del Gaudio, and R. Lanari (2006), Surface deformation analysis in the Ischia Island (Italy) based on spaceborne radar interferometry, *J. Volcanol. Geotherm. Res.*, *151*, 399–416.

McNamara, D. E., et al. (2015), Reactivated faulting near Cushing, Oklahoma: Increased potential for a triggered earthquake in an area of United States strategic infrastructure, *Geophys. Res. Lett.*, *42*, 1944–8007, doi:10.1002/2015GL064669.

Mulargia, F., and A. Bizzarri (2014), Anthropogenic triggering of large earthquakes, *Nat. Sci. Rep.*, *4*, 6100, doi:10.1038/srep06100.

Okada, Y. (1985), Surface deformation due to shear and tensile faults in a half-space, *Bull. Seismol. Soc. Am.*, *75*(4), 1135–1154.

Okada, Y. (1992), Internal deformation due to shear and tensile faults in a half-space, *Bull. Seismol. Soc. Am.*, *82*(2), 1018–1040.

Rabus, B., M. Eineder, A. Roth, and R. Bamler (2003), The Shuttle Radar Topography Mission—A new class of digital elevation models acquired by spaceborne radar, *Photogramm. Remote Sens.*, *57*, 241–262.

Samsonov, S., and N. d'Oreye (2012), Multidimensional time series analysis of ground deformation from multiple InSAR data sets applied to Virunga Volcanic Province, *Geophys. J. Int.*, *191*(3), 1095–1108, doi:10.1111/j.1365-246X.2012.05669.x.

Samsonov, S., N. d'Oreye, and B. Smets (2013), Ground deformation associated with post-mining activity at the French-German border revealed by novel InSAR time series method, *Int. J. Appl. Earth Obs. Geoinf.*, *23*, 142–154.

Samsonov, S. V., P. Gonzalez, K. Tiampo, and N. d'Oreye (2014a), Modeling of fast ground subsidence observed in southern Saskatchewan (Canada) during 2008–2011, *Nat. Hazards Earth Syst. Sci.*, *14*, 247–257, doi:10.5194/nhess-14-247-2014.

Samsonov, S. V., N. d'Oreye, P. González, K. Tiampo, L. Ertolahti, and J. Clague (2014b), Rapidly accelerating subsidence in the Greater Vancouver region from two decades of ERS-ENVISAT-RADARSAT-2 DInSAR measurements, *Remote Sens. Environ.*, *143*(5), 180–191, doi:10.1016/j.rse.2013.12.017.

Samsonov, S. V., K. F. Tiampo, A. G. Camacho, J. Fernández, and P. J. González (2014c), Spatiotemporal analysis and interpretation of 1993–2013 ground deformation at Campi Flegrei, Italy, observed by advanced DInSAR, *Geophys. Res. Lett.*, *41*, 6101–6108, doi:10.1002/2014GL060595.

Samsonov, S. V., A. P. Trishchenko, K. Tiampo, P. J. González, Y. Zhang, and J. Fernández (2014d), Removal of systematic seasonal atmospheric signal from interferometric synthetic aperture radar ground deformation time series, *Geophys. Res. Lett.*, *41*, 6123–6130, doi:10.1002/2014GL061307.

Samsonov, S., M. Czarnogorska, and D. White (2015), Satellite interferometry for high-precision detection of ground deformation at a carbon dioxide storage site, *Int. J. Greenhouse Gas Control*, *42*, 188–199, doi:10.1016/j.ijggc.2015.07.034.

Samsonov, S., K. Tiampo, and W. Feng (2016), Fast subsidence in downtown of Seattle observed with satellite radar, *Remote Sens. Appl. Soc. Environ.*, *4*, 179–187, doi:10.1016/j.rsase.2016.10.001.

Sarychikhina, O., E. Glowacka, R. Mellors, and F. S. Vidal (2011), Land subsidence in the Cerro Prieto Geothermal Field, Baja California, Mexico, from 1994 to 2005. An integrated analysis of DInSAR, leveling and geological data, *J. Volcanol. Geotherm. Res.*, *204*(1–4), 76–90, doi:10.1016/j.jvolgeores.2011.03.004.

Segall, P., J.-R. Grasso, and A. Mossop (1994), Poroelastic stressing and induced seismicity near the Lacq gas field, southwestern France, *J. Geophys. Res.*, *99*(B8), 15,423–15,438, doi:10.1029/94JB00989.

Shirzaei, M., W. Ellsworth, K. Tiampo, P. González, and M. Manga (2016), Surface uplift and time-dependent seismic hazard due to fluid injection in eastern Texas, *Science*, *353*(6306), 1416–1419, doi:10.1126/science.aag0262.

Simpson, R., and P. Reasenberg (1994), Earthquake-induced static stress changes on central California faults, in *The Loma Prieta, California, Earthquake of October 17, 1989: Tectonic Processes and Models, U.S. Geol. Surv. Prof. Pap. 1550-F.*, edited by R. W. Simpson, pp. F55–F89, U.S. Geol. Surv., Washington, D. C.

Trugman, D., A. Borsa, and D. Sandwell (2014), Did stresses from the Cerro Prieto Geothermal Field influence the El Mayor-Cucapah rupture sequence?, *Geophys. Res. Lett.*, *41*, 8767–8774, doi:10.1002/2014GL061959.

Wackerly, D., W. Mendenhall, and R. Scheaffer (2007), *Mathematical Statistics With Applications*, 7th ed., Duxbury Press, Boston, Mass.

Wang, K., and Y. Fialko (2014), Space geodetic observations and models of postseismic deformation due to the 2005 M7.6 Kashmir (Pakistan) earthquake, *J. Geophys. Res. Solid Earth*, *119*, 7306–7318, doi:10.1002/2014JB011122.

Ward, S., and S. Barrientos (1986), An inversion for slip distribution and fault shape from geodetic observations of the 1983, Borah Peak, Idaho, earthquake, *J. Geophys. Res.*, *91*, 4909–4919.

Wegmuller, U., and C. Werner (1997), GAMMA SAR processor and interferometry software. paper presented at 3rd ERS symposium on space at the service of our environment, Florence, Italy.

Wei, S., et al. (2011), Superficial simplicity of the 2010 El Mayor-Cucapah earthquake of Baja California in Mexico, *Nat. Geosci.*, *4*, 615–618, doi:10.1038/NGEO1213.

Yamagiwa, S., S. Miyazaki, K. Hirahara, and Y. Fukahata (2015), Afterslip and viscoelastic relaxation following the 2011 Tohoku-oki earthquake (M_w 9.0) inferred from inland GPS and seafloor GPS/acoustic data, *Geophys Res. Lett.*, *42*, 1944–8007, doi:10.1002/2014GL061735.